

Spintronics for image recognition: Performance benchmarking via ultrafast data-driven simulations

Anatole MOUREAUX,^{1, a)} Chloé CHOPIN,¹ Laurent JACQUES,² and Flavio ABREU ARAUJO^{1, b)}

¹⁾*Institute of Condensed Matter and Nanosciences, Université catholique de Louvain, Place Croix du Sud 1, 1348 Louvain-la-Neuve, Belgium*

²⁾*Institute for Information and Communication Technologies, Electronics and Applied Mathematics, Université catholique de Louvain, Avenue Georges Lemaître 4, 1348 Louvain-la-Neuve, Belgium*

We present a demonstration of image classification using an echo-state network (ESN) relying on a single simulated spintronic nanostructure known as the vortex-based spin-torque oscillator (STVO) delayed in time. We employ an ultrafast data-driven simulation framework called the data-driven Thiele equation approach (DD-TEA) to simulate the STVO dynamics. This allows us to avoid the challenges associated with repeated experimental manipulation of such a nanostructured system. We showcase the versatility of our solution by successfully applying it to solve classification challenges with the MNIST, EMNIST-letters and Fashion MNIST datasets. Through our simulations, we determine that within a large ESN the results obtained using the STVO dynamics as an activation function are comparable to the ones obtained with other conventional nonlinear activation functions like the ReLU and the sigmoid. While achieving state-of-the-art accuracy levels on the MNIST dataset, our model's performance on EMNIST-letters and Fashion MNIST is lower due to the relative simplicity of the system architecture and the increased complexity of the tasks. We expect that the DD-TEA framework will enable the exploration of deeper architectures, ultimately leading to improved classification accuracy.

I. INTRODUCTION

The impact of artificial intelligence (AI) on various industries and our daily lives has been transformative. It has facilitated critical functions such as medical image recognition for early disease diagnosis and optimization of manufacturing processes^{1,2}. However, the widespread use of AI has raised concerns about its energy consumption and environmental impact during resource-intensive training and large-scale inference phases³. To address these challenges, growing efforts to develop energy-efficient alternatives with cutting-edge performance are underway. Moreover, conventional computers, despite decades of miniaturization and optimization, are nearing their limits in computing power^{4,5}.

In response to these challenges, novel approaches in artificial intelligence have emerged, aiming to surpass the limitations of digital frameworks. One such solution is echo-state networks (ESNs), which involve randomly injecting data into a layer of nonlinearly activated units called a reservoir⁶. This process projects the input data into a higher-dimensional space, easing, under certain conditions, the linear separability of the reservoir's outputs. Notably, only the weights of the readout layer need optimization, leaving the reservoir weights unchanged. Furthermore, the readout training step amounts to a mere linear regression, hence significantly reducing the training time compared to traditional algorithms relying on gradient descent and error backpropagation. As the learning step can be performed in a single shot over the whole training set, ESNs offer the advantage of finding a global minimum of the loss function, ensuring determinism and reproducibility⁷. The fixed nature of the reservoir makes it well-suited

for hardware implementations, enabling the creation of dedicated hardware analog processors to optimize performance and energy efficiency⁸. Research has also demonstrated that such reservoirs can be implemented using a single nonlinear unit delayed in time without sacrificing performance⁹⁻¹¹, by trading on the execution time. This feature, called time-multiplexing, further eases the hardware implementation of such applications.

Efficient data classification through physical reservoir computing has been demonstrated in various works, utilizing optoelectronic systems^{12,13} as well as nonlinear oscillators known as vortex-based spin-torque oscillators¹⁴ (STVOs). STVOs are nanometer-sized magnetic tunnel junctions (MTJs) that rely on spintronics to operate¹⁵. Spin electronics, also referred to as spintronics, describe the physical phenomena related to the transport of spin in magnetic materials and nanostructures.

The ground state magnetization of STVOs is a magnetic vortex, composed of in-plane curling magnetization, at the center of which is located the out-of-plane magnetization vortex core (see Fig. 1a). When an electric current is injected into a STVO, the vortex core undergoes circular oscillations in the plane of the MTJ due to an effect called the spin-transfer torque^{14,16,17} (STT) (pink circular arrow in Fig. 1). Thanks to another phenomenon referred to as tunnel magnetoresistance¹⁸ (TMR), stable oscillations of the electrical resistance and of the voltage in the MHz range are obtained. By utilizing an amplitude-modulated signal as input (Fig. 1b), these voltage oscillations display a nonlinear amplitude with respect to the input signal amplitude¹⁹, as represented in Fig. 1c. This nonlinearity is also represented in the time-varying reduced position of the vortex core $s(t) = ||X(t)||/R$, where $||X(t)||$ is the time-dependent position of the vortex core in the plane of the MTJ and R is its radius²⁰. STVOs offer numerous advantages, such as low power consumption, minimal noise and compatibility with complementary metal-oxide-semiconductor (CMOS) technology²¹, mak-

^{a)}anatole.moureaux@uclouvain.be

^{b)}flavio.abreuaraujo@uclouvain.be; <https://flavio.be>

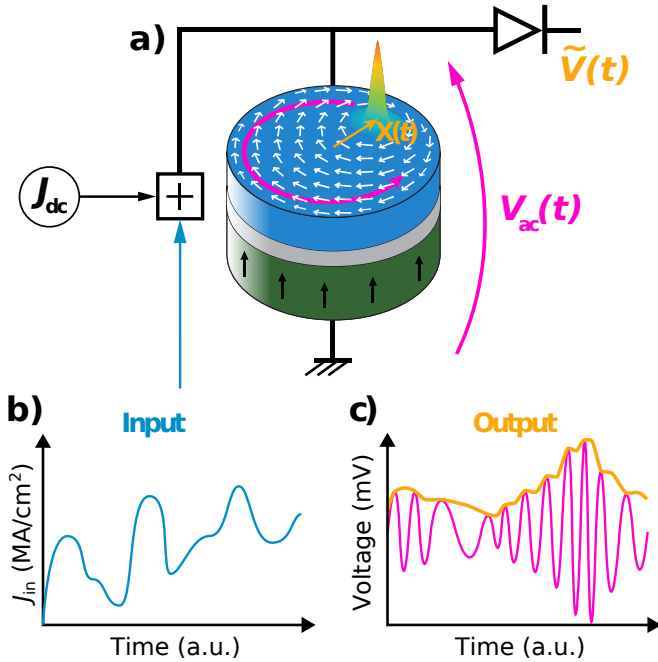


FIG. 1. (a) Radio-frequency oscillations of the vortex core reduced position $s(t)$ are triggered by (b) the injection of an amplitude-modulated signal $J_{in}(t)$ in the STVO. A bias current density J_{dc} is added to the input signal in order to trigger oscillations of the vortex core. (c) The non-linearity of $s(t)$ can be retrieved experimentally by recording the envelope $\tilde{V}(t)$ of the voltage $V_{ac}(t)$ across the oscillator (best seen in color).

ing them attractive candidates for nonlinear data transformation in neuromorphic applications^{22–25}.

Despite the progress in STVO-based hardware computing systems, a significant challenge lies in their development, optimization and testing due to the laborious and costly process of manipulating such nanostructures repeatedly. To overcome these limitations, simulating STVOs and their complex dynamics proves to be a more feasible approach. Micromagnetic simulations²⁶ (MMS) offer highly accurate results but are time and energy-consuming, making them impractical for simulating and optimizing STVO-based neuromorphic applications. A computationally lighter alternative is the Thiele equation approach (TEA), which employs a single ordinary differential equation for each space direction to model STVO dynamics²⁷. TEA is unfortunately merely qualitative in the steady (resp. transient) oscillatory state *i.e.*, when the magnetization undergoes stable oscillations (resp. switches from a stable state to another one). Both of these states are however crucial for nonlinearly transforming data^{20,25}.

A recent solution to this challenge is the data-driven Thiele equation approach (DD-TEA) developed by Abreu Araujo *et al.*²⁰. This semi-analytical model accurately describes the STVO dynamics in both steady and transient states by using numerical parameters extracted from a small set of MMS. Consequently, DD-TEA enables STVO simulation with the same level of accuracy as MMS but with a significant acceleration factor of 9 orders of magnitude²⁸.

The present study showcases the ability of a simulated STVO-based ESN to achieve state-of-the-art accuracy for image classification on the MNIST dataset. Firstly, we will introduce our implementation of a time-multiplexed echo state network (ESN) using a single STVO delayed in time. The data preprocessing and training procedures will be detailed. Next, we will explain how we simulate the STVO dynamics and the ESN using the DD-TEA framework. Subsequently, we will evaluate the network’s performance in classifying various types of images, such as handwritten digits from MNIST²⁹, characters from EMNIST-letters³⁰ and clothing items from Fashion MNIST³¹ (FMNIST). The STVO dynamics will then be compared to more conventional nonlinear functions, the ReLU and the sigmoid functions. The role of the nonlinearity in such a system will also be highlighted. Those studies will be carried for various numbers of virtual nodes in the ESN reservoir to demonstrate the potential of DD-TEA for efficient hyperparameters assessment.

II. METHODS

A. Time-multiplexed ESN using a single STVO delayed in time

ESNs consist in encoding the input data by randomly projecting them into a higher-dimension space, and then transforming the projected data nonlinearly. The results of this nonlinear random projection can then be mapped to the final output of the network using a multiplication with a weight matrix learned by linear regression during the training phase. This output matrix is the only set of parameters in the network that needs optimization. Our system architecture is depicted in Fig. 2, and is equivalent to the simple-chain ESN multiplexed in time presented in ref.¹⁰.

During inference, each image from the MNIST dataset is first converted from its initial shape (28×28) into a column vector \mathbf{x} of 784 pixels whose grayscale intensity value spans from 0 to 255. We reduce each flattened image to a vector \mathbf{x}' of size N_f where each value is the weighted sum of \mathbf{x} and the N_f most significant directions \mathbf{C} in the training set extracted with principal component analysis^{32,33} (PCA). This allows to select only the N_f linear combinations of each image’s pixels that explain the most variance in the training set, and hence helps to denoise and reduce the dimensionality of the input data. This operation is represented by Eq. 1 and Fig. 2. We choose to select only the 44 most significant directions, as it already allows to explain 80% of the variance in the training set.

$$\mathbf{x}' = \mathbf{C}\mathbf{x} \quad (1)$$

Then, each resulting vector \mathbf{x}' is encoded in a random space of dimension N_θ using a multiplication with a random mask \mathbf{M} whose value are uniformly distributed in the $[-1;1]$ interval (Eq. 2 and Fig. 2). As \mathbf{M} is fixed, all the projected data \mathbf{x}'' belong to the same random space.

$$\mathbf{x}'' = \mathbf{M}\mathbf{x}' \quad (2)$$

The projected data \mathbf{x}'' are nonlinearly transformed using the STVO dynamics. To do so, each \mathbf{x}'' is transformed to a current density $J_{\text{in},\mathbf{x}''}$ and added to the bias current density J_{dc} . Then, each resulting signal is injected into a STVO, and the resulting

reduced position of the vortex core s is simulated and recorded as output. To simplify our implementation, we only use a single STVO delayed in time instead of N_θ distinct oscillators, a technique referred to as time-multiplexing^{11,25,34,35}. The reduced position $s(t)$ of the vortex core is recorded every D_t nanoseconds. D_t is chosen shorter than the characteristic time of the STVO transient state to ensure that the dynamics is always nonlinear. This step is represented by Eq. 3 and the central part of Fig. 2.

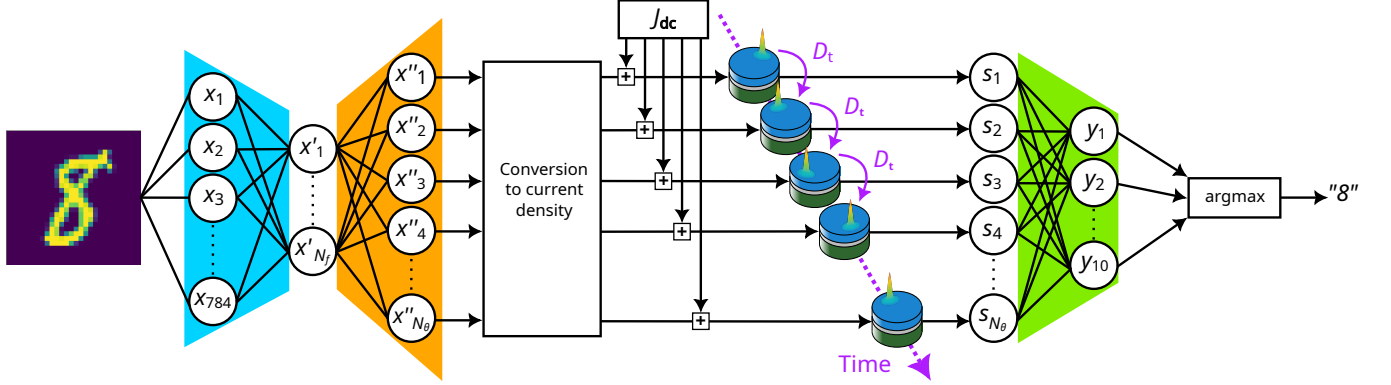


FIG. 2. Time-multiplexed ESN using a single STVO delayed in time for image recognition. The blue part represents the denoising process using PCA. The orange part represents higher-dimension random encoding. The resulting encoded signals are converted into current density and injected in a single STVO for nonlinear transformation. The output of the STVO is mapped to the final output using weights learned by linear regression over the training set.

$$\mathbf{s} = \begin{bmatrix} s(J_{\text{in},\mathbf{x}''}(D_t) + J_{\text{dc}}) \\ s(J_{\text{in},\mathbf{x}''}(2D_t) + J_{\text{dc}}) \\ \dots \\ s(J_{\text{in},\mathbf{x}''}(N_\theta D_t) + J_{\text{dc}}) \end{bmatrix} \quad (3)$$

After that, the recorded reduced positions are mapped to the output of the network using the weights \mathbf{W}_{out} learned during the training phase, as represented by Eq. 4 and the green part of Fig. 2. The final computed target \hat{i} representing the category of the input data is obtained by using the argmax function (Eq. 5).

$$\mathbf{y} = \mathbf{W}_{\text{out}}\mathbf{s} \quad (4)$$

$$\hat{i} = \text{argmax}(\mathbf{y}) \quad (5)$$

The weight matrix \mathbf{W}_{out} is retrieved by using a linear regression between the STVO outputs for the 60000 samples of the training set $\mathbf{S}_{\text{train}} = [\mathbf{s}_{\text{train},i}]$ and the corresponding vectorized targets $\mathbf{T}_{\text{train}} = [\mathbf{t}_{\text{train},i}]$ for i ranging from 1 to 60000. Standard algorithms such as ridge regression can be used, so that the regularization parameter can be tuned accordingly to the problem to avoid overfitting. In our case, the Moore-Penrose pseudo-inverse^{36,37} matrix $\mathbf{S}_{\text{train}}^\dagger$ is considered (Eq. 6).

$$\mathbf{W}_{\text{out}} = \mathbf{T}_{\text{train}}\mathbf{S}_{\text{train}}^\dagger \quad (6)$$

B. Modeling the STVO dynamics

The reduced position of the vortex core $s(t)$ can be analytically modeled within the DD-TEA^{20,28} framework using

Eq. 10. In this equation, D_t (in nanoseconds) represents the sampling period of the input signal $J_{\text{in},\mathbf{x}''}(t)$ and the rate at which it is sent into the STVO. The parameters $\alpha(J_{\text{in},\mathbf{x}''}(t))$, $\beta(J_{\text{in},\mathbf{x}''}(t))$ and $n(J_{\text{in},\mathbf{x}''}(t))$ are derived from the TEA and rule the time-dependent nonlinearity of the STVO dynamics. In the DD-TEA framework, they are polynomials fitted to values obtained through MMS^{20,28} (Eqs. 7, 8 and 9). The reduced position $s(J_{\text{in},\mathbf{x}''}(t))$ incorporates the past position $s(J_{\text{in},\mathbf{x}''}(t - D_t))$ to capture the intrinsic short-term memory implemented by the STVO dynamics. In the context of reservoir computing, the model described in Eq. (10) serves as the internal nonlinear function implemented by the virtual STVOs in the reservoir.^{6,8,12,13,25,34}

$$\alpha(J_{\text{in},\mathbf{x}''}(t)) = 6.64J_{\text{in},\mathbf{x}''}(t) - 39.97 \quad (7)$$

$$\beta(J_{\text{in},\mathbf{x}''}(t)) = -0.43J_{\text{in},\mathbf{x}''}(t) - 25.92 \quad (8)$$

$$\begin{aligned} n(J_{\text{in},\mathbf{x}''}(t)) = & -95.97J_{\text{in},\mathbf{x}''}(t) + 25.54J_{\text{in},\mathbf{x}''}(t)^2 \\ & - 2.87J_{\text{in},\mathbf{x}''}(t)^3 + 0.18J_{\text{in},\mathbf{x}''}(t)^4 \\ & + 157.14 \end{aligned} \quad (9)$$

$$s(J_{\text{in},\mathbf{x}''}(t)) = \frac{s(J_{\text{in},\mathbf{x}''}(t - D_t))}{\sqrt[n(J_{\text{in},\mathbf{x}''}(t))]{\left(1 + \frac{J_{\text{in},\mathbf{x}''}(t - D_t)^{n(J_{\text{in},\mathbf{x}''}(t))}}{\alpha(J_{\text{in},\mathbf{x}''}(t))/\beta(J_{\text{in},\mathbf{x}''}(t)})\right)} \exp(-n(J_{\text{in},\mathbf{x}''}(t))\alpha(J_{\text{in},\mathbf{x}''}(t))D_t) - \frac{s(t - D_t)^{n(J_{\text{in},\mathbf{x}''}(t))}}{\alpha(J_{\text{in},\mathbf{x}''}(t))/\beta(J_{\text{in},\mathbf{x}''}(t))}} \quad (10)$$

C. Generalizability and performance benchmarking

To assess the generalizability of our implementation of simulated hardware reservoir computing, the training and inference processes described in the previous part are applied on two additional image datasets. The first one is the EMNIST-letters dataset: an extension of MNIST to handwritten letters³⁰. It consists of 124,800 training images and 20,800 testing images, classified into 26 classes corresponding to the 26 letters in the alphabet. Each class contains lower and upper case letters. The second dataset is Fashion MNIST (FMNIST³¹) and is composed of 60,000 training images and 10,000 testing images, all extracted from the Zalando website. The images are separated into 10 classes representing clothing items: {*t-shirt/top*, *trouser*, *pullover*, *dress*, *coat*, *sandal*, *shirt*, *sneaker*, *bag*, *ankle boot*}.

The performance of our time-multiplexed STVO-based ESN at classifying images from the MNIST, EMNIST-letters and FMNIST datasets will be assessed as follows. A STVO-based ESN will be trained with each dataset accordingly to the procedure described in the previous section. The number of PCA components selected will be chosen to ensure an explained variance of 80%. This allows to reduce the dimension of the data from 784 to $N_f = 38$ (resp. $N_f = 24$) for the EMNIST-letters (resp. FMNIST) dataset. The accuracy (the ratio of correctly classified samples in the testing dataset) and the normalized root-mean-square error (NRMSE) between each predicted output \mathbf{y} and the corresponding target \mathbf{t} defined as $\text{NRMSE} := \left(\frac{\|\mathbf{y} - \mathbf{t}\|^2}{\|\mathbf{t}\|^2}\right)^{1/2}$ will be averaged over the entire testing set of each dataset. To decrease the influence of the randomness of \mathbf{M} , the metrics will be averaged over 10 iterations using different randomly generated versions of \mathbf{M} . The process will be repeated for an increasing number of virtual neurons in the nonlinear layer (*i.e.*, an increasing N_θ). This will show the potential of DD-TEA for performing extensive parametric studies and optimizing such hyperparameters.

Finally, the performance will be compared to the same architecture with more conventional nonlinear transfer functions such as the ReLU and the sigmoid functions. This will be achieved by artificially replacing Eq. (10) by the corresponding expressions in the simulations. The identity function will also be tested as an activation function to assess the role of the nonlinearity in the learning ability of the ESN.

III. RESULTS

The accuracy and the NRMSE of our STVO-based ESN is depicted for the MNIST dataset in Fig. 3. Without surprise, the accuracy (resp. NRMSE) increases (resp. decreases) with an increasing number of nodes in the nonlinear layer. As a matter of fact, the number of nodes is directly proportional to the number of tunable parameters in the model (*i.e.*, the number of elements in the learned matrix \mathbf{W}). The shaded areas on the plots represent the range where the input data \mathbf{x} is projected into a smaller dimension space due to the low amount of virtual nodes in the nonlinear layer (*i.e.*, $N_\theta < N_f$). The projection hence compresses information instead of projecting it into a higher dimension space.

Above this limit, the absence of nonlinearity in the identity function leads to a saturation of the performance at the exact same value (see the red curve in Fig. 3). Indeed once $N_\theta \geq N_f$, the input data are linearly interpolated by the network parameters (\mathbf{W}_{out}), and no additional performance gain can be expected by further increases of N_θ . Considering a linear transfer function represented by $s(\mathbf{x}'') = k\mathbf{x}''$, the classification process of an input \mathbf{x} can be summarized by

$$\hat{t} = \arg\max \left(\mathbf{T}_{\text{train}} \mathbf{S}_{\text{train}}^\dagger k \mathbf{M} \mathbf{C} \mathbf{x} \right). \quad (11)$$

By substituting $\mathbf{S}_{\text{train}}$ by $k \mathbf{M} \mathbf{C} [\mathbf{x}_{\text{train},i}]_{60000}^1$, Eq. 11 transforms to

$$\begin{aligned} \hat{t} &= \arg\max \left(\mathbf{T}_{\text{train}} (k \mathbf{M} \mathbf{C} [\mathbf{x}_{\text{train},i}]_{60000}^1)^\dagger k \mathbf{M} \mathbf{C} \mathbf{x} \right) \\ &= \arg\max \left(\mathbf{T}_{\text{train}} ([\mathbf{x}_{\text{train},i}]_{60000}^1)^\dagger (k \mathbf{M} \mathbf{C})^\dagger k \mathbf{M} \mathbf{C} \mathbf{x} \right). \end{aligned} \quad (12)$$

As $(k \mathbf{M} \mathbf{C})^\dagger (k \mathbf{M} \mathbf{C}) \simeq \mathbf{I}^{38}$, one finally gets Eq. (13), which is independent of k , \mathbf{C} and \mathbf{M} , and hence of the network internal parameters.

$$\hat{t} = \arg\max \left(\mathbf{T}_{\text{train}} ([\mathbf{x}_{\text{train},i}]_{60000}^1)^\dagger \mathbf{x} \right) \quad (13)$$

In all the cases, the accuracy and the NRMSE tend to a common value for all the nonlinear activation functions ($s(J_{\text{in},\mathbf{x}''})$, ReLU and sigmoid). This implies that the STVO dynamics nonlinearity is equivalent to that of these more conventional functions. This also indicates that the nature of the nonlinearity is not determinant in the case of an ESN when the number of learnable parameters (proportional to N_θ) becomes high. However, any form of nonlinearity is still required to improve the quality of the data classification when $N_\theta > N_f$ as showed

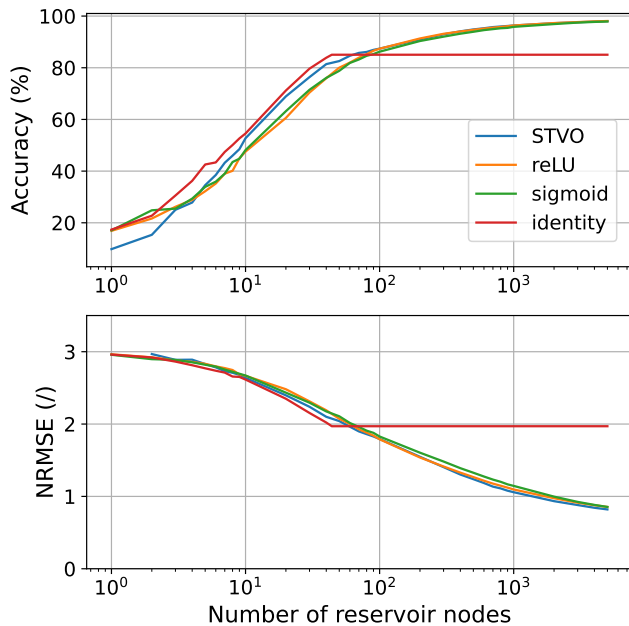


FIG. 3. Accuracy and NRMSE of our time-multiplexed ESN on the MNIST dataset for an increasing number of nodes. The nonlinear transfer function of the reservoir nodes is set with the STVO dynamics and the reLU and sigmoid functions. Linear nodes are also tested using the identity function.

by the high performance gap between the nonlinear functions and the identity function.

The comparison of the accuracy of the classification using the STVO-based ESN for the three datasets is represented in Fig. 4. It can be seen that for a very low number of virtual nodes in the reservoir, the accuracy reaches the random choice (*i.e.*, 10% for MNIST and FMNIST, and 3.85% for EMNIST-letters). The accuracy eventually reaches an accuracy of 98% on MNIST and an accuracy of 88.4% (resp. 86.9%) on the EMNIST-letters (resp. FMNIST) dataset with 5000 nodes in the nonlinear layer. We believe that the relatively low score achieved in FMNIST is due to the lack of convolutional treatment of the input features, something that is known to be of prior importance for complex images classification. Concerning EMNIST-letters, we suspect that the lower quality of the recognition is due to the presence of lower case and upper case characters in each category, which can be regarded as the presence of two distinct datasets with the same labels. This assumption is consolidated by computing the average intra-class variance in each dataset. The variance of each class \mathbf{K} is computed accordingly to $\text{Var}_{\text{intra}}(\mathbf{K}) = (\sum_i (\mathbf{x}_i - \bar{\mathbf{K}})^2) / |\mathbf{K}|$ and averaged over all the classes for each dataset. It is equal to 3452.9 in MNIST, 4408.7 in EMNIST-letters and 3401 in FMNIST. The average intraclass variance is about 28% bigger in EMNIST-letters than in MNIST and FMNIST.

For comparison, the top accuracy reached on MNIST known to this day is 99.87%³⁹. While our solution performs better than other reservoir computing-based approaches (in software and hardware)^{40–42}, other works indicate that higher

performance could be achieved by increasing further the number of nodes in the reservoir⁴³. The top accuracy on EMNIST-letters and FMNIST are respectively 95.96% and 96.91%^{44,45}. However, these works are based on neural networks far more complex than our, involving many specialized layers such as convolutional layers and attention modules. Therefore, these solutions are not currently suited for hardware integration within a neuromorphic system.

IV. CONCLUSION

We designed an echo-state network based on hardware nonlinear spintronics oscillators called STVOs. This neuromorphic system aims at solving cognitive tasks more energy-efficiently than conventional software solutions. The system has a simple architecture and only requires the learning of a small part of the involved parameters. Moreover, the learning can be performed by simply using the Moore-Penrose pseudoinverse, and all the nonlinear treatment of the data takes place in a fixed and random reservoir.

To overcome the limitations inherent to experimentally developing, optimizing and testing such a nanostructured system, we used ultrafast STVO simulation. This model yields an explicit expression for the STVO dynamics that we used as neuronal nonlinearity. This approach allows to simulate an entire STVO-based ESN accurately at ultra-high speed compared to previously available frameworks.

We showed that a STVO-based ESN is able to classify images of handwritten digits from the MNIST dataset with state-of-the-art accuracy levels. Indeed, the nonlinearity of STVO dynamics is equivalent to more conventional nonlinearities such as the reLU and the sigmoid functions. Moreover, the system is generalizable to other problems such as the EMNIST-letters and the fashion MNIST datasets. We suspect

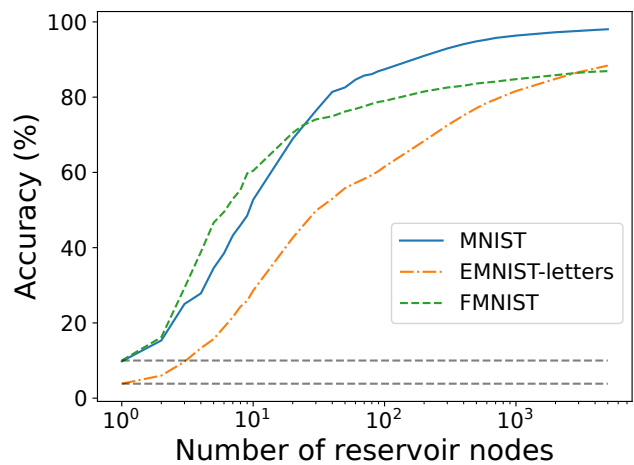


FIG. 4. Accuracy of the STVO-based ESN for the MNIST, EMNIST-letters and FMNIST datasets. The dashed lines represent the random choice accuracy levels linked to the number of categories in each dataset ($100\%/26 = 3.85\%$ and $100\%/10 = 10\%$).

that better performance can be obtained on the two latter tasks by designing a more specialized architecture, for example involving convolutional data treatment before the reservoir⁴⁶.

The use of the DD-TEA framework allowed to carry on extensive studies of the performance with respect to the number of reservoir nodes. This could be reproduced with other hyperparameters such as the input and output shapes of the data or the properties of the input matrix \mathbf{M} . Physical operating parameters having an influence on the STVO dynamics could also be optimized by doing so, allowing an efficient preparation of an experimental setup.

We expect that STVO-based ESNs can be successfully used for other tasks, such as time series prediction. Moreover, we think that DD-TEA could allow to develop and test other neural architectures involving STVOs, and investigate other types of learning rules to perform complex machine learning tasks with increased efficiency.

V. ACKNOWLEDGEMENTS

Computational resources have been provided by the Consortium des Équipements de Calcul Intensif (CÉCI), funded by the Fonds de la Recherche Scientifique de Belgique (F.R.S.-FNRS) under Grant No. 2.5020.11 and by the Walloon Region. F.A.A. is a Research Associate of the F.R.S.-FNRS. Heartfelt thanks to Simon de Wergifosse for his insights and helpful discussions.

VI. REFERENCES

- ¹W. Sun, B. Zheng, and W. Qian, in *Medical imaging 2016: computer-aided diagnosis*, Vol. 9785 (SPIE, 2016) pp. 241–248.
- ²D. S. Leme, S. A. da Silva, B. H. G. Barbosa, F. M. Borém, and R. G. F. A. Pereira, *Computers and electronics in agriculture* **156**, 312 (2019).
- ³P. Dhar, *Nat. Mach. Intell.* **2**, 423 (2020).
- ⁴M. V. Wilkes, *ACM SIGARCH Computer Architecture News* **23**, 4 (1995).
- ⁵D. J. Frank, R. H. Dennard, E. Nowak, P. M. Solomon, Y. Taur, and H.-S. P. Wong, *Proceedings of the IEEE* **89**, 259 (2001).
- ⁶M. Lukoševičius and H. Jaeger, *Computer science review* **3**, 127 (2009).
- ⁷B. Schrauwen, D. Verstraeten, and J. Van Campenhout, in *Proceedings of the 15th european symposium on artificial neural networks*, p. 471-482 (2007) pp. 471–482.
- ⁸G. Tanaka, T. Yamane, J. B. Héroux, R. Nakane, N. Kanazawa, S. Takeda, H. Numata, D. Nakano, and A. Hirose, *Neural Networks* **115**, 100 (2019).
- ⁹L. Appeltant, M. C. Soriano, G. Van der Sande, J. Danckaert, S. Massar, J. Dambre, B. Schrauwen, C. R. Mirasso, and I. Fischer, *Nature communications* **2**, 468 (2011).
- ¹⁰S. Ortín, M. C. Soriano, L. Pesquera, D. Brunner, D. San-Martín, I. Fischer, C. Mirasso, and J. Gutiérrez, *Scientific reports* **5**, 14945 (2015).
- ¹¹M. Borghi, S. Biasi, and L. Pavesi, *Scientific Reports* **11**, 15642 (2021).
- ¹²L. Larger, M. C. Soriano, D. Brunner, L. Appeltant, J. M. Gutiérrez, L. Pesquera, C. R. Mirasso, and I. Fischer, *Optics express* **20**, 3241 (2012).
- ¹³Y. Paquot, F. Duport, A. Smerieri, J. Dambre, B. Schrauwen, M. Haelterman, and S. Massar, *Scientific reports* **2**, 287 (2012).
- ¹⁴V. Pribiag, I. Krivorotov, G. Fuchs, P. Braganca, O. Ozatay, J. Sankey, D. Ralph, and R. Buhrman, *Nature physics* **3**, 498 (2007).
- ¹⁵Y. Gaididei, V. P. Kravchuk, and D. D. Sheka, *International Journal of Quantum Chemistry* **110**, 83 (2010).
- ¹⁶D. C. Ralph and M. D. Stiles, *Journal of Magnetism and Magnetic Materials* **320**, 1190 (2008).
- ¹⁷K. Y. Guslienko, O. V. Sukhostavets, and D. V. Berkov, *Nanoscale research letters* **9**, 1 (2014).
- ¹⁸S. Yuasa and D. Djayaprawira, *Journal of Physics D: Applied Physics* **40**, R337 (2007).
- ¹⁹F. Abreu Araujo, C. Chopin, and S. de Wergifosse, *Scientific Reports* **12**, 10605 (2022).
- ²⁰F. Abreu Araujo, C. Chopin, and S. de Wergifosse, *arXiv preprint arXiv:2206.13596* (2022), 10.48550/arXiv.2206.13596.
- ²¹K. Yogendra, D. Fan, and K. Roy, *IEEE Transactions on Magnetics* **51**, 1 (2015).
- ²²J. Torrejon, M. Riou, F. Abreu Araujo, S. Tsunegi, G. Khalsa, D. Querlioz, P. Bortolotti, V. Cros, K. Yakushiji, A. Fukushima, *et al.*, *Nature* **547**, 428 (2017).
- ²³M. Romera, P. Talatchian, S. Tsunegi, F. Abreu Araujo, V. Cros, P. Bortolotti, J. Trastoy, K. Yakushiji, A. Fukushima, H. Kubota, *et al.*, *Nature* **563**, 230 (2018).
- ²⁴D. Marković, N. Leroux, M. Riou, F. Abreu Araujo, J. Torrejon, D. Querlioz, A. Fukushima, S. Yuasa, J. Trastoy, P. Bortolotti, *et al.*, *Applied Physics Letters* **114** (2019), 10.1063/1.5079305.
- ²⁵F. Abreu Araujo, M. Riou, J. Torrejon, S. Tsunegi, D. Querlioz, K. Yakushiji, A. Fukushima, H. Kubota, S. Yuasa, M. D. Stiles, *et al.*, *Scientific reports* **10**, 328 (2020).
- ²⁶J. Leliaert and J. Mulkers, *Journal of Applied Physics* **125** (2019), 10.1063/1.5093730.
- ²⁷A. Thiele, *Physical Review Letters* **30**, 230 (1973).
- ²⁸A. Moureaux, S. de Wergifosse, C. Chopin, J. Weber, and F. Abreu Araujo, *arXiv preprint arXiv:2301.11025* (2023), 10.48550/arXiv.2301.11025.
- ²⁹L. Deng, *IEEE Signal Processing Magazine* **29**, 141 (2012).
- ³⁰G. Cohen, S. Afshar, J. Tapson, and A. Van Schaik, in *2017 international joint conference on neural networks (IJCNN)* (IEEE, 2017) pp. 2921–2926.
- ³¹H. Xiao, K. Rasul, and R. Vollgraf, *arXiv preprint arXiv:1708.07747* (2017), 10.48550/arXiv.1708.07747.
- ³²M. Ringér, *Nature biotechnology* **26**, 303 (2008).
- ³³S. Karamzadeh, S. M. Abdullah, A. A. Manaf, M. Zamani, and A. Hooman, *Journal of Signal and Information Processing* **4**, 173 (2013).
- ³⁴L. Larger, A. Baylón-Fuentes, R. Martinenghi, V. S. Udaltsov, Y. K. Chembo, and M. Jacquot, *Physical Review X* **7**, 011015 (2017).
- ³⁵M. Riou, F. Abreu Araujo, J. Torrejon, S. Tsunegi, G. Khalsa, D. Querlioz, P. Bortolotti, V. Cros, K. Yakushiji, A. Fukushima, *et al.*, in *2017 IEEE International Electron Devices Meeting (IEDM)* (IEEE, 2017) pp. 36–3.
- ³⁶P. Courrieu, *arXiv preprint arXiv:0804.4809* (2008), 10.48550/arXiv.0804.4809.
- ³⁷J. C. A. Barata and M. S. Hussein, *Brazilian Journal of Physics* **42**, 146 (2012).
- ³⁸A. Ben-Israel and T. N. Greville, *Generalized inverses: theory and applications*, Vol. 15 (Springer Science & Business Media, 2003).
- ³⁹A. Byerly, T. Kalganova, and I. Dear, *Neurocomputing* **463**, 545 (2021).
- ⁴⁰S. D. Gardner, M. R. Haider, L. Moradi, and V. Vantsevich, in *2021 IEEE International Midwest Symposium on Circuits and Systems (MWS-CAS)* (IEEE, 2021) pp. 255–258.
- ⁴¹R. Zhu, A. Loeffler, J. Hochstetter, A. Diaz-Alvarez, T. Nakayama, A. Stieg, J. Gimzewski, J. Lizier, and Z. Kuncic, in *International Conference on Neuromorphic Systems 2021* (2021) pp. 1–4.
- ⁴²S. D. Gardner and M. R. Haider, *IEEE Journal on Flexible Electronics* **1**, 185 (2022).
- ⁴³N. Schaetti, M. Salomon, and R. Couturier, in *2016 IEEE Intl conference on computational science and engineering (CSE) and IEEE Intl conference on embedded and ubiquitous computing (EUC) and 15th Intl symposium on distributed computing and applications for business engineering (DCABES)* (IEEE, 2016) pp. 484–491.
- ⁴⁴P. Jeevan, K. Viswanathan, and A. Sethi, *arXiv preprint arXiv:2205.14375* (2022), 10.48550/arXiv.2205.14375.
- ⁴⁵M. S. Tanveer, M. U. K. Khan, and C.-M. Kyung, in *2020 25th International Conference on Pattern Recognition (ICPR)* (IEEE, 2021) pp. 4789–4796.
- ⁴⁶Z. Tong and G. Tanaka, in *2018 24th International Conference on Pattern Recognition (ICPR)* (IEEE, 2018) pp. 1289–1294.